Dual-species quantum degeneracy of ^{40}K and ^{87}Rb on an atom chip

M. H. T. Extavour, L. J. LeBlanc, T. Schumm, B. Cieslak, S. Myrskog, A. Stummer, S. Aubin, J. H. Thywissen

Department of Physics and Institute for Optical Sciences, University of Toronto, 60 St. George Street, Toronto, Canada

Abstract. In this article we review our recent experiments with a ^{40}K-^{87}Rb mixture. We demonstrate rapid sympathetic cooling of a ^{40}K-^{87}Rb mixture to dual quantum degeneracy on an atom chip. We also provide details on efficient BEC production, species-selective magnetic confinement, and progress toward integration of an optical lattice with an atom chip. The efficiency of our evaporation allows us to reach dual degeneracy after just 6 s of evaporation - more rapidly than in conventional magnetic traps. When optimizing evaporative cooling for efficient evaporation of ^{87}Rb alone we achieve BEC after just 4 s of evaporation and an 8 s total cycle time.

Keywords: Ultracold atoms, Bose-Einstein condensation, degenerate Fermi gas, sympathetic cooling, atom chips, species-selective potentials, microfabrication
PACS: 39.25.+k, 34.20.-b, 32.80.Pj, 3.75.Ss, 3.75.Nt, 85.40.Hp

INTRODUCTION

Ultra-cold gases of neutral fermionic atoms are of great interest in atomic and condensed matter physics, yet they remain challenging to produce experimentally. This article describes the production and manipulation of ultra-cold fermionic and bosonic gases using an atom chip and a simple, single-chamber vacuum system. We describe the observation of efficient evaporation to a Bose-Einstein condensate (BEC) in ^{87}Rb, along with the rapid sympathetic evaporative cooling of a ^{40}K-^{87}Rb mixture to dual degeneracy - a BEC of ^{87}Rb and a degenerate Fermi gas (DFG) of ^{40}K. We discuss the use of radio frequency (RF) dressed potentials to create species-selective magnetic microtraps. Finally, we detail progress toward incorporating an optical lattice into our experiment. Although some of the details of our setup and DFG-BEC have been reported elsewhere [1, 2], this article provides an overview and update on important figures of merit.

The article begins with an outline of our initial optical and magnetic trapping and cooling stages for ^{87}Rb and ^{40}K. Next, we give a description of our observation of quantum degeneracy in both species, and further details of our evaporative cooling trajectories. We then describe the use of RF-dressed adiabatic potentials to produce a species-selective microtrap. The article ends with a discussion of our plans to integrate optical lattices into the experiment, and a discussion of the technical improvements being made to our atom chip.
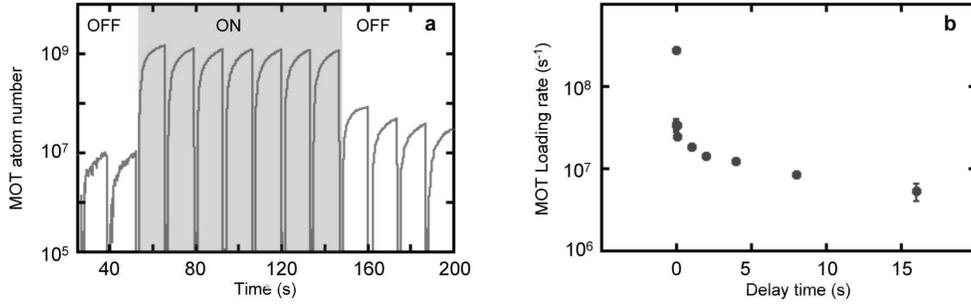
FIGURE 1. MOT loading via LIAD We load the MOT from the atomic vapour formed via light-induced atomic desorption (LIAD) from the interior walls of our Pyrex vacuum cell. (**a**) As the ^{87}Rb MOT is repeatedly loaded from atomic vapour, we observe a one-hundred-fold increase in atom number (greyed area), which is lost after the LEDs are switched off. (**b**) The MOT loading rate as function of time *after* the LEDs have been switched off. Once the LEDs are off, the MOT loading rate undergoes a sharp initial decrease from the LED-on value of 3×10^8 s^{-1}, followed by a slower decay to the LED-off value of $\sim 10^6$ s^{-1} in approximately 300 s.

LOADING AND TRAPPING

We begin by trapping neutral atoms directly from atomic vapour with a six-beam magneto-optical trap (MOT). The dual species MOT consists of two overlapping sets beams: six counterpropagating beams at 780 nm to trap ^{87}Rb, and six beams at 767 nm for ^{40}K [1]. With ^{87}Rb MOT loading times as short at 950 ms, we can achieve BEC . Working with the ^{40}K-^{87}Rb mixture requires longer loading times due to the low isotopic abundance of ^{40}K in our dispensers[1]: we first load ^{40}K alone into the MOT for 10-20 s, after which ^{87}Rb is loaded for an additional 1-5 s, while maintaining the ^{40}K population. Both sets of MOT beams operate with a detuning of -26 MHz until the last 10 ms of the load, when the ^{40}K is compressed by reducing the detuning of the ^{40}K beams to -10 MHz. With this procedure we load 10^9 ^{87}Rb atoms and 10^7 ^{40}K atoms into the MOT.

The background atomic ^{87}Rb and ^{40}K vapours are enhanced via light-induced desorption (LIAD) of alkali atoms from the inner walls of a 75 mm $\times$ 75 mm $\times$ 165 mm rectangular Pyrex vacuum cell [1]. By illuminating the cell using approximately 600 mW of incoherent 405 nm LED light[2], we observe a 100-fold increase in ^{87}Rb MOT atom number compared to loading from the background vapour alone (see Figure 1). The increase in ^{40}K MOT atom number is unknown; we cannot observe a ^{40}K MOT without LIAD. A coating of ^{87}Rb and ^{40}K atoms on the interior walls of our vacuum chamber is replenished every few weeks by running a commercial Rb dispenser and a home-made K dispenser.

After MOT loading, 3 ms of optical molasses cooling is applied to the ^{87}Rb. Finally, both species are optically pumped into weak-field-seeking hyperfine ground states: $|F = 2, m_F = 2\rangle$ for ^{87}Rb and $|F = 9/2, m_F = 9/2\rangle$ for ^{40}K.

---

[1] We use KCl powder whose ^{40}K isotopic abundance has been enriched to 5% from the naturally-occurring 0.012%. For comparison, the natural abundance of ^{87}Rb is 28%.

[2] We use ten Epitex L405 series UV illuminators.

We use a magnetic transfer procedure to transport the atoms from the site of the MOT to the atom chip, the site of evaporative cooling. Immediately following optical pumping, all optical fields are extinguished and atoms are confined in a two-coil quadrupole magnetic trap formed at the site of the MOT. A biasing magnetic field generated by a third coil shifts the magnetic trap centre vertically to just below the surface of the atom chip, which is mounted horizontally in the vacuum chamber 5 cm above the MOT site.

Once near the surface of the atom chip, atoms are smoothly transferred from the quadrupole magnetic trap into an anisotropic, Ioffe-Pritchard-type magnetic microtrap. The chip trap is formed by combining the static magnetic fields generated by DC current in a 'Z'-shaped wire on the atom chip with an external, uniform magnetic field parallel to the chip surface [3]. This combination produces a non-zero magnetic field minimum just below the chip surface, in which atoms in weak-field-seeking hyperfine states are confined. Atoms are transferred into the microtrap by ramping up the Z-wire current and external field while ramping down the quadrupole trap.

QUANTUM DEGENERACY

We cool to quantum degeneracy using forced RF evaporative cooling of ^{87}Rb. Whether cooling ^{87}Rb alone or a ^{40}K-^{87}Rb mixture [4, 5, 6], RF radiation acts only on the ^{87}Rb, ejecting hot atoms from the magnetic trap and allowing the remaining atoms to rethermalize to a new, lower temperature. The the process of indirectly cooling the one species by direct RF evaporation of the other is referred to as sympathetic cooling [7, 8, 9, 10, 11]. In our case ^{40}K is cooled indirectly via thermalizing elastic collisions with the ^{87}Rb.

Evaporative cooling of bosons alone. In the ^{87}Rb-only case we achieve a BEC of 2×10^5 atoms when empirically optimizing for evaporation efficiency. We first load the MOT for 2 s, magnetically trap and transfer to the chip in 950 ms, and load atoms into a chip microtrap in 310 ms at $T \sim 300\ \mu$K. Next, we perform forced RF evaporative cooling in which the RF frequency ν_{RF} is swept from 15.0 MHz to 3.6 MHz in 4.3 s, bringing the the total cycle time to ~ 7.6 s. Evaporation is carried out in an anisotropic trap with trap frequencies of $\omega_\perp/2\pi = 560$ Hz and $\omega_\ell/2\pi = 32$ Hz. The log-slope efficiency η_{evap} of the evaporation, defined as $-\partial[log(\rho)]/\partial[log(N)]$, where ρ is the phase space density[3] and N the atom number, is equal to 4.0 ± 0.1 when we optimize evaporation for ^{87}Rb alone. For comparison, $\eta_{evap} = 2.9 \pm 0.4$ when evaporation is optimized for sympathetic cooling to dual degeneracy (see Figure 2). Our largest BECs are achieved with cycle times of 15 s, and contain 3×10^5 atoms.

When optimizing for minimum cycle time, we sacrifice some evaporation efficiency, but achieve a BEC of 2×10^4 atoms with cycle times as short as 5.7 s. In this case, we load the MOT for 950 ms, and transfer to the atom chip as described above. Evaporative cooling is carried out in two empirically optimized steps. The initial 700 ms RF

---

[3] Phase space density is defined as $n_0\lambda_{dB}^3$ in this context, where n_0 is the peak atomic density, and λ_{dB} the thermal deBroglie wavelength.
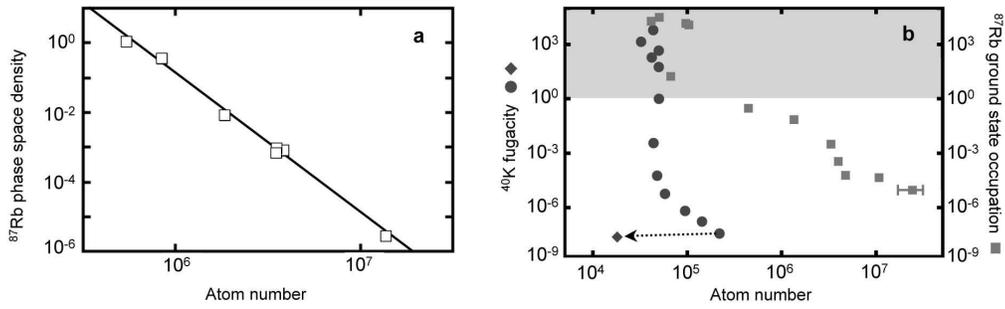
FIGURE 2.   Evaporative cooling in a chip trap. (**a**) The ^{87}Rb evaporative cooling trajectory optimized for ^{87}Rb alone is more efficient than that used for sympathetic cooling. The line of best fit establishes the log-slope efficiency (defined in the text). (**b**) Spin-polarized fermions without a bosonic bath cannot be evaporatively cooled (diamond). However, if bosonic ^{87}Rb (squares) is evaporatively cooled, then fermionic ^{40}K is sympathetically cooled (circles) to quantum degeneracy (greyed area). For bosonic ^{87}Rb, the vertical axis is the occupation of the ground state; for fermionic ^{40}K, the vertical axis is the fugacity. These two quantities are equivalent in the non-degenerate limit. A typical run-to-run spread in atom number is shown on the right-most point; all vertical error bars are smaller than the marker size.

frequency sweep from $\nu_{RF} = 33.5$ MHz to $\nu_{RF} = 6.0$ MHz is carried out in a compressed trap, which has $\omega_\perp/2\pi = 2.8$ kHz at its centre and a transverse magnetic field gradient of 4800 G/cm at its edge. Next, the microtrap is decompressed until $\omega_\perp/2\pi = 861$ Hz and $\omega_\ell/2\pi = 32$ Hz. A second evaporative ν_{RF} sweep is carried out here, from 27.9 MHz to 3.5 MHz in 2030 ms.

We detect the phase transition from thermal gas to BEC by tracking the peak phase space density of the gas. We fit time-of-flight absorption images with a composite peak function to capture the separate behaviour of the condensed and non-condensed fractions: a Thomas-Fermi parabola describes the condensate fraction, and a Bose function non-condensed fraction (see Figure 3f). These fits yield reliable atom number and temperature data, from which we determine the phase (thermal atoms or BEC) of the cloud. Once below T_c we also observe an inversion in the aspect ratio of the expanding cloud [12]. Figures 3e-g show absorption images of expanding condensates at three successively colder temperatures: above T_c, where the gas is entirely non-condensed; near T_c, where the BEC begins to emerge; and much below T_c, where the condensed fraction dominates the cloud.

Sympathetic cooling of the Bose-Fermi mixture.   When working with the ^{40}K-^{87}Rb mixture, we find that RF sweep times faster than ~ 6 s are not successful in achieving dual degeneracy. This is because the ^{40}K-^{87}Rb rethermalization time lags that of ^{87}Rb-^{87}Rb at high temperatures. This empirical observation was studied in the context of the Ramsauer-Townsend effect in [2]. We are also unable to sympathetically cool in the compressed trap used for rapid BEC production, since the higher densities in this trap lead to three-body loss, preventing efficient cooling of the ^{40}K-^{87}Rb mixture [4, 6]. Figure 2 shows the relative evaporation efficiencies ^{87}Rb and ^{40}K during sympathetic cooling, as well as during single-species evaporation of ^{87}Rb alone.

We first load 2×10^5 ^{40}K and 2×10^7 ^{87}Rb doubly spin-polarized atoms into a 1.1 mK-deep microtrap at a temperature $\gtrsim 300\,\mu$K. The ^{40}K radial and longitudinal trapping
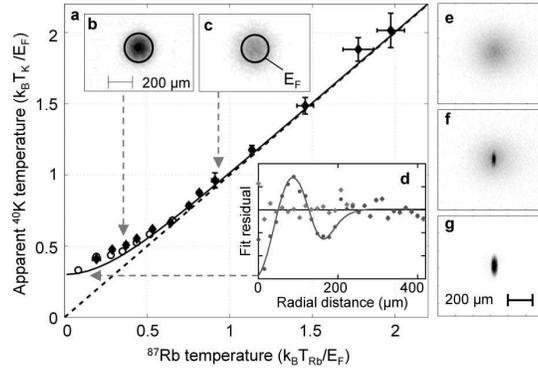
FIGURE 3. Observation of Fermi statistics. Due to Fermi pressure, Fermi degenerate ^{40}K clouds appear to stop getting colder, even when the reservoir temperature approaches zero. (**a**) The apparent temperature of the fermions, as measured by Gaussian fits to images of ^{40}K clouds, is plotted versus temperature of both thermal (diamonds) and Bose-condensed (circles) ^{87}Rb. Data is compared to a Gaussian fit of a theoretically generated ideal Fermi distribution (solid line) and its classical expectation (dashed line). Both temperatures are scaled by the Fermi energy E_F of each ^{40}K cloud. Error bars are statistical (one standard deviation), with uncertainty smaller than the sizes of symbols for lower temperature data. Absorption images are shown for $k_B T/E_F = 0.35$ (**b**) and 0.95 (**c**), including a circle indicating the Fermi energy E_F. (**d**) A closer look at the fermion cloud shape reveals that it does not follow a Boltzmann distribution. The fit residuals of a radially averaged cloud profile show a strong systematic deviation when assuming Boltzmann (circles) instead of Fermi (diamonds) statistics. A degenerate Fermi cloud is flatter at its centre than a Boltzmann distribution, and falls more sharply to zero near its edge. (**e-g**) Absorption images of ^{87}Rb atoms after 20 ms of time-of-flight expansion: above (**e**), just below (**f**), and well below T_c (**g**), which shows 2.5×10^5 atoms in a quasi-pure BEC. $T_c \approx 400$ nK in this data. The BEC is anisotropic in-trap, with its long axis aligned horizontally. This alignment is inverted at long times of flight as evident in these images.

frequencies are measured to be $\omega_\perp/2\pi = 826 \pm 7\,\mathrm{Hz}$ and $\omega_\ell/2\pi = 46.2 \pm 0.7\,\mathrm{Hz}$, respectively[4]. ν_{RF} is swept from 28.6 MHZ to 3.6 MHz in 6.15 s.

As with ^{87}Rb, we assess the degree of quantum degeneracy in ^{40}K by fitting absorption data with ideal gas theory. In the case of ^{40}K, fits using ideal fermion density distributions yield temperature, density, Fermi energy and fugacity. However, since there is no phase transition to the quantum degenerate state in cold, spin-polarized non-interacting fermions, distinguishing degenerate from non-degenerate Fermi gases is much more challenging. Nevertheless, we observe a clear signature of Fermi degeneracy in ^{40}K below $T \approx 1\,\mu$K in the shape of the time-of-flight distribution.

We compare the rms cloud sizes of the ^{40}K and the non-condensed ^{87}Rb fraction by fitting the density profiles to the Gaussian shapes predicted by Boltzmann statistics. Figure 3a shows that the apparent (i.e., Gaussian-estimated) ^{40}K temperature approaches a finite value while the ^{87}Rb temperature approaches zero, even though the two gases are in good thermal contact. This deviation is evidence of the Fermi pressure expected of a gas obeying Fermi-Dirac statistics, and of the Pauli exclusion prin-

---

[4] The corresponding ^{87}Rb trap frequencies are a factor of $\sqrt{m_{Rb}/m_K} \approx 1.47$ smaller than those for ^{40}K, where m_{Rb} and m_K are the atomic masses of ^{87}Rb and ^{40}K, respectively.

ciple [13]: at zero temperature, fermions fill all available energy states up to the Fermi energy $E_F = \hbar(6N\omega_\perp^2\omega_\ell)^{1/3}$, where N is the number of fermions. We plot data with thermal (diamonds) and Bose-condensed (circles) ^{87}Rb separately, to show that the density-dependent attractive interaction between ^{40}K and ^{87}Rb does not significantly affect the release energy. For our typical parameters, $E_F \approx k_B \times 1.1\,\mu$K. After all ^{87}Rb atoms have been evaporated, we use Fermi-Dirac fits to measure temperature, and find $k_B T / E_F$ as low as 0.09 ± 0.05 with as many as 4×10^4 ^{40}K atoms.

SPECIES-SELECTIVE MICROTRAPS

A common practice among experimental realizations of ^{40}K-^{87}Rb mixtures [4, 6, 5] (and Bose-Fermi mixtures generally) is the use of a single potential which confines both species. The ability to separately control the external potential of each species is a new and useful tool for studying such mixtures, which we demonstrate here. Tunable, species-selective magnetic confinement of our ^{40}K-^{87}Rb mixture is accomplished by combining a transverse field oscillating at radio frequency (RF) with the static magnetic microtrap [14, 15, 16, 17, 18].

When the RF frequency is resonant with the magnetic hyperfine splitting of one atomic species, the RF radiation induces a coupling between the m_F levels in that species, just as in forced RF evaporative cooling. Unlike in evaporative cooling, however, we ramp the RF frequency from *below* to *above* resonance. Doing so dynamically transforms the potential from the $|F = 2, m_F = 2\rangle$ single-well (ν_{RF} below resonance) into a dressed state double-well (ν_{RF} above resonance)[5]. The central barrier height and well separation of the double-well are controlled by the RF frequency and amplitude [16].
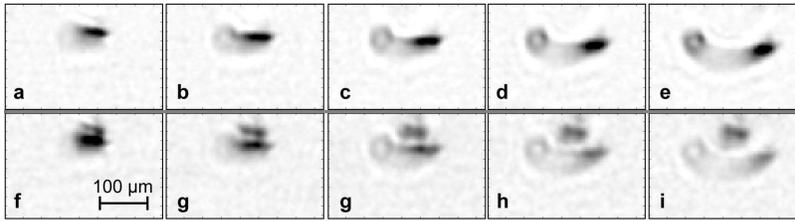
We achieve species-selective dressed potentials when the RF radiation is resonant to the ground state hyperfine splitting of ^{87}Rb, but well detuned from that of ^{40}K. In a magnetic field the energy separation between the five $F = 2$ hyperfine levels in the $5^2S_{1/2}$ ^{87}Rb ground state is roughly twice the separation of that between the ten $F = 9/2$ hyperfine levels in the $4^2S_{1/2}$ ^{40}K ground state[6]. The ^{87}Rb double well is formed by increasing the RF frequency from 3.6 MHz to a final RF frequency between 4.0 MHz and 6.0 MHz (see Figure 4). The single-well ^{87}Rb static trap deforms into a double-well as the RF frequency passes through the ^{87}Rb trap bottom, located at 3.8 MHz, while the ^{40}K potential remains almost unaffected by the RF dressing: we estimate the Rabi frequency Ω_R to be as high as 1 MHz, whereas the static magnetic bias field provides a minimum detuning of 2.1 MHz between ^{40}K and ^{87}Rb resonances.

Figure 4 shows absorption images of the ^{40}K-^{87}Rb mixture 0.3 ms after being released from the RF-dressed trap. As expected, the ^{87}Rb atoms split primarily into two clouds as the double-well RF frequency is increased. The ^{40}K atoms, still experiencing the bare static trap, remain confined to a single, central cloud. This species separation

---

[5] In evaporative cooling, the RF frequency is ramped down starting from *above* resonance, so that atoms experience a single-well dressed state potential at all times during evaporation.

[6] $U_{magnetic} = m_F g_F \mu_B B$, where μ_B is the Bohr magneton and B the magnitude of magnetic field. The Landé g-factor g_F is $2/9$ for $F{=}9/2$ in ^{40}K and $1/2$ for $F = 2$ in ^{87}Rb.

FIGURE 4. Species-selective manipulation. A static chip trap loaded with a ^{40}K-^{87}Rb mixture is coupled to an RF field to induce a double-well dressed potential for ^{87}Rb only; the ^{40}K portion of the mixture remains unsplit. The final RF coupling frequency increases from 4.0 MHz (**a** and **e**) to 6.0 MHz (**f** and **i**) in steps of 0.5 MHz, deforming the ^{87}Rb dressed potential minimum. (**a-e**) Absorption images of the mixture with probe light resonant to ^{87}Rb only. (**f-i**) Absorption images of the mixture taken with two-colour probe light resonant to both species. Both species are visible, with the ^{40}K atoms nearly unaffected by the RF dressing.

was observed via absorption imaging with a two-colour probe beam, the two optical frequencies corresponding to the imaging transitions in ^{87}Rb and ^{40}K.

NEXT GENERATION ATOM CHIP: ON-CHIP OPTICAL LATTICES

With an eye to future experiments, we are in the midst of developing a new atom chip which can support an optical lattice. The atom chip will be covered by a dielectric mirror, enabling the formation of a 1D optical lattice near the chip surface with a single, retroreflected laser beam. Improved chip optical access will allow the incorporation of additional beams to form 2D and 3D lattices.

Mirrorizing is carried out following Reichel's replica technique [19]. Once the chip wires have been fabricated on the substrate, a planarizing epoxy is applied to the atom chip. A dielectric mirror on a glass substrate is then carefully lowered onto the epoxy layer, pressed, and held in place while the epoxy cures. Once the epoxy has set and cured, the mirror substrate is carefully removed, leaving the smooth dielectric mirror adhered to the atom chip.

The new atom chip will also contain smoother wires with higher current capacity, fabricated with photolithography, evaporative deposition, and lift-off. The chip substrate is an AlN wafer with filled vias connecting the front (wire) side to the backside of the chip. This allows for electrical contacts to be made on the back side of the chip, removing them as obstacles and thus greatly increasing our optical access. After evaporative deposition of Cr and Ti adhesion layers, a 2.7 μm-thick layer of Ag and a thin capping layer of Au are evaporated directly onto the substrate to form the chip wires. Evaporative deposition was chosen over electroplating to reduce the wire roughness, which in turn will reduce the rugosity of the resulting magnetic potential [20, 21, 22]. High DC current capacity in these wires is enabled by the combination of the high electrical conductivity of Ag and the high thermal conductivity of AlN. Recent tests have shown that as much as 7.5 A of current can be passed through a 20 μm-wide, 2.7 μm-tall, 4.6 mm-long wire; this corresponds to a current density of greater than 10^7 A/cm^2.

ACKNOWLEDGMENTS

REFERENCES

1. S. Aubin, M. H. T. Extavour, S. Myrskog, L. J. LeBlanc, J. Estève, S. Singh, P. Scrutton, D. McKay, R. McKenzie, I. Leroux, A. Stummer, and J. H. Thywissen, *J. Low Temp. Phys.* **140**, 377–396 (2005).
2. S. Aubin, S. Myrskog, M. H. T. Extavour, L. J. LeBlanc, D. McKay, A. Stummer, and J. H. Thywissen, *Nature Physics* **2**, 384 (2006).
3. J. Reichel, *Appl. Phys. B* **75**, 469–487 (2002).
4. G. Roati, F. Riboli, G. Modugno, and M. Inguscio, *Phys. Rev. Lett.* **89**, 150403 (2002).
5. J. Goldwin, S. Inouye, M. L. Olsen, B. Newman, B. D. DePaola, and D. S. Jin, *Phys. Rev. A* **70**, 021601 (2004).
6. C. Ospelkaus, S. Ospelkaus, K. Sengstock, and K. Bongs, *Phys. Rev. Lett.* **96**, 020401 (2006).
7. Z. Hadzibabic, C. A. Stan, K. Dieckmann, S. Gupta, M. W. Zwierlein, A. Görlitz, and W. Ketterle, *Phys. Rev. Lett.* **88**, 160401 (2002).
8. C. J. Myatt, E. A. Burt, R. W. Ghrist, E. A. Cornell, and C. E. Wieman, *Phys. Rev. Lett.* **78**, 586–589 (1997).
9. F. Schreck, G. Ferrari, K. L. Corwin, J. Cubizolles, L. Khaykovich, M. O. Mewes, and C. Salomon, *Phys. Rev. A* **64**, 011402 (2001).
10. S. Inouye, J. Goldwin, M. L. Olsen, C. Ticknor, J. L. Bohn, and D. S. Jin, *Phys. Rev. Lett.* **93**, 183201 (2004).
11. F. Ferlaino, C. D'Errico, G. Roati, M. Zaccanti, M. Inguscio, G. Modugno, and A. Simoni, *Phys. Rev. A* **73**, 040702 (2006).
12. W. Ketterle, D. S. Durfee, and D. M. Stamper-Kurn, "Making, probing and understanding Bose-Einstein condensates," in *Bose-Einstein Condensation in Atomic Gases*, edited by C. E. W. M. Inguscio, S. Stringari, IOS Press, Amsterdam, Oxford, Washington DC, 1998, Proceedings of the International School of Physics "Enrico Fermi", pp. 67–176.
13. A. G. Truscott, K. E. Strecker, W. I. McAlexander, G. B. Partridge, and R. G. Hulet, *Science* **291**, 2570–2572 (2001).
14. O. Zobay, and B. M. Garraway, *Phys. Rev. Lett.* **86**, 1195–1198 (2001).
15. Y. Colombe, E. Knyazchyan, O. Morizot, B. Mercier, V. Lorent, and H. Perrin, *Europhys. Lett.* **67**, 593–599 (2004).
16. T. Schumm, S. Hofferberth, L. M. Wildermuth, S. Groth, I. Bar-Joseph, J. Schmiedmayer, and P. Kruger, *Nature Physics* **1**, 57–62 (2005).
17. P. W. Courteille, B. Deh, J. Fortágh, A. Günter, S. Kraft, C. Marzok, S. Slama, and C. Zimmermann, *J. Phys. B* **39**, 1055 (2006).
18. M. White, H. Gao, M. Pasienski, and B. DeMarco, *arXiv:cond-mat/0605393* (2006).
19. J. Reichel, W. Hänsel, P. Hommelhoff, and T. W. Hänsch, *Appl. Phys. B* **72**, 81–89 (2001).
20. J. Fortágh, H. Ott, S. Kraft, A. Günter, and C. Zimmermann, *Phys. Rev. A* **66**, 041604 (2002).
21. J. Estève, C. Aussibal, T. Schumm, C. Figl, D. Mailly, I. Bouchoule, C. I. Westbrook, and A. Aspect, *Phys. Rev. A* **70**, 043629 (2004).
22. S. Groth, P. Krüger, S. Wildermuth, R. Folman, T. Fernholz, J. Schmiedmayer, D. Mahalu, and I. Bar-Joseph, *Appl. Phys. Lett.* **85**, 2980–2982 (2004).